Land-sea temperature contrasts at the Last Interglacial and their impact on the hydrological cycle

Nicholas King-Hei Yeung[1,2], Laurie Menviel[1], Katrin J. Meissner[1,2], Andréa S. Taschetto[1,2], Tilo Ziehn[3], and Matthew Chamberlain[4]

[1]Climate Change Research Centre, University of New South Wales, Sydney NSW, Australia
[2]ARC Centre of Excellence for Climate Extremes, University of New South Wales, Sydney NSW, Australia
[3]CSIRO Oceans and Atmosphere, Aspendale VIC, Australia
[4]CSIRO Oceans and Atmosphere, Hobart TAS, Australia

Correspondence: Nicholas K. H. Yeung (nicholas.yeung@unsw.edu.au)

Abstract. Due to different orbital configurations, high northern latitude summer insolation was higher during the Last Interglacial period (LIG; 129–116 thousand years before present, ka) than during the preindustrial period (PI), while high southern latitude summer insolation was lower. The climatic response to these changes is studied here with focus on the Southern Hemisphere monsoons, by performing an equilibrium experiment of the LIG at 127 ka with the Australian Earth System Model, ACCESS-ESM1.5, as part of the Paleoclimate Model Intercomparison Project 4 (PMIP4). Simulated mean surface air temperature between 40° N and 60° N over land during boreal summer is 6.5 °C higher at the LIG compared to PI, which leads to a northward shift of the Inter-Tropical Convergence Zone (ITCZ) and a strengthening of the North African and Indian monsoons. Despite 0.4 °C cooler conditions in austral summer in the Southern Hemisphere (0–90° S), annual mean air temperatures are 1.2 °C higher at southern mid-to-high latitudes (40° S–80° S). These differences in temperature are coincident with a large-scale reorganisation of the atmospheric circulation. The ITCZ shifts southward in the Atlantic and Indian sectors during the LIG austral summer compared to PI, leading to increased precipitation over the southern tropical oceans. However, weaker Southern Hemisphere insolation during LIG austral summer induces a significant cooling over land, which in turn weakens the land-sea temperature contrast, leading to an overall reduction (−20 %) in monsoonal precipitation over the Southern Hemisphere's continental regions compared to PI. The intensity and areal extent of the Australian, South American and South African monsoons are consistently reduced in LIG. This is associated with greater pressure and subsidence over land due to a strengthening of the Southern Hemisphere Hadley cell during austral summer.

1 Introduction

Antarctic ice cores suggest that the Last Interglacial period (LIG; ∼129–116 thousand years before present (ka)), also known as Marine Isotope Stage 5e or the Eemian, was most likely the warmest interglacial of the last 800 ka (Masson-Delmotte et al., 2013). Paleoproxy records suggest that annual mean sea surface temperatures (SSTs) were about ∼0.5 °C (Hoffman et al., 2017) to ∼1.1 °C (Capron et al., 2017) above preindustrial (PI) values at the LIG in the North Atlantic. The summer warming at high northern latitudes on land was particularly pronounced with estimated temperatures 4 to 5 °C above PI (CAPE-Last

Interglacial Project Members, 2006) and a 3 to 11 °C warming over Greenland (NEEM community members et al., 2013; Landais et al., 2016). It has also been suggested that LIG Southern Ocean SSTs were ∼1.8 °C higher than PI (Capron et al., 2017).

Global mean sea-level was ∼6 to 9 m higher during the LIG than the PI (Kopp et al., 2009; Dutton and Lambeck, 2012), with Greenland ice sheets contributing 0.6 to 3.5 m (Dutton et al., 2015), and an Antarctic ice-sheet contribution likely greater than 6 m (Kopp et al., 2009; Rohling et al., 2019). Despite its importance, there are still a lot of uncertainties associated with the processes leading to ice-mass loss at the LIG. Even though paleoproxy records provide constraints on the LIG climate, low spatial and temporal resolution and uncertainties in transfer functions add uncertainties to the climate response to LIG boundary conditions. Numerical simulations of the LIG can thus improve our understanding of the climate processes and feedbacks at play.

The LIG equilibrium simulation (lig127k) is one of the highest-priority experiments of the Paleoclimate Modeling Inter-comparison Project 4 (PMIP4) designated simulations in the Coupled Model Intercomparison Project (CMIP6) (Otto-Bliesner et al., 2017). It primarily aims to examine the climate response due to changes in orbital configuration at a time when atmo-spheric greenhouse gas concentrations and continental configurations were similar to PI (Table 1). At the LIG, the Earth's orbit had a larger eccentricity, with the timing of perihelion closer to the boreal summer solstice (Berger, 1978). Together with a greater axial tilt of the Earth, it led to higher insolation north of 40° S between April and September, with a maximum anomaly of ∼70 W m^{-2} at high northern latitudes in June. Insolation was generally lower south of 60° N between October and March and particularly in the Southern Hemisphere (SH) in December and January, with insolation anomalies reaching −45 W m^{-2} compared to PI (Fig. 1).

A recent study presented the large-scale features of the PMIP4-CMIP6 lig127k experiment as deduced from 17 participat-ing climate models (Otto-Bliesner et al., 2021). Compared to PI, strong warming is shown over Northern Hemisphere (NH) continents during June, July, and August (JJA), while a cooling is simulated in December, January, and February (DJF), due to the seasonal character of insolation anomalies (Otto-Bliesner et al., 2021). This leads to a substantial reduction in the boreal summer Arctic sea-ice extent, while there is little change in maximum sea-ice area during winter (Kageyama et al., 2021). The multi-model study by Kageyama et al. (2021) is in broad agreement with available paleoproxy records showing that regions south of 78° N in the Atlantic and Nordic Seas were seasonally ice-free, though model-data comparison north of 78° N is difficult due to ambiguous interpretations of proxy data.

The PMIP4 lig127k ensemble mean shows that boreal summer monsoonal precipitation is enhanced over northern Africa (and extends into Saudi Arabia), India and southeast Asia, and northwestern Mexico, while in the SH, austral summer mon-soonal precipitation decreases over Australia, southern Africa and South America (Otto-Bliesner et al., 2021). Although the model spread for precipitation is large, the models generally agree on the sign of change in area-averaged monsoonal precip-itation, except for the South Asian and Australian monsoons. While studies based on proxy records consistently demonstrate a strengthening of the African and Indian monsoons (e.g. Magiera et al., 2019; Orland et al., 2019; Rohling et al., 2002), the precipitation changes in SH are less clear. A compilation of LIG precipitation proxy records with near-global coverage and a multi-model-data comparison are presented in Scussolini et al. (2019). The study includes 138 sites based on a range of proxies.

Most of the data suggest an increase in NH annual mean precipitation during the LIG relative to the PI, with the exception of a small number of individual proxy sites. In the SH, the proxy signal is less consistent and spatially heterogeneous, with only partial model-data agreement.

In this study we present the large-scale climatic features of the LIG equilibrium experiment (lig127k) as simulated by the ACCESS-ESM1.5 model, compared to the preindustrial experiment (Ziehn et al., 2020), and to available paleoproxy records. We also explore the changes in austral summer precipitation in the SH.

2 Model description and experimental design

2.1 ACCESS-ESM1.5 model description

ACCESS-ESM1.5 (Ziehn et al., 2020) is an updated version of ACCESS-ESM1 (Law et al., 2017). The differences between ACCESS-ESM1.5 and ACCESS-ESM1 are relatively small, with the majority of the changes concerning the land surface and ocean model.

The atmospheric component of the ACCESS-ESM1.5 is the UK Met Office Unified Model version 7.3 (UM7.3; Martin et al., 2010; The HadGEM2 Development Team et al., 2011), but with the Community Atmosphere Biosphere Land Exchange model (CABLE2.4; Kowalczyk et al., 2013) as land surface model. The ocean component is the NOAA/ GFDL Modular Ocean Model version 5 (MOM5; Griffies, 2014) with the same configuration as the ocean model component of ACCESS1.0 and ACCESS1.3 (Bi et al., 2012). Sea ice is simulated using the LANL CICE4.1 model (Hunke and Lipscomb, 2010), which has the same horizontal grid as the ocean with 5 thickness classes. Coupling of the ocean and sea-ice to the atmosphere is achieved through the OASIS-MCT coupler (Valcke, 2013). The physical climate model configuration used here is similar to the ACCESS1.3 model, which contributed to the Coupled Model Intercomparison Project Phase 5 (CMIP5) (Bi et al., 2012). The spatial resolutions of model components are listed in Table 1.

The carbon cycle is included in ACCESS through the Nutrient, Phytoplankton, Zooplankton and Detritus (NPZD) model WOMBAT (World Ocean Model of Biogeochemistry and Trophic dynamics; Oke et al., 2013), and through the land surface model CABLE and its biogeochemistry module CASA-CNP (Wang et al., 2010), with CASA-CNP being run with nitrogen and phosphorus limitation.

In the CABLE configuration applied here, there are a total of 13 plant functional types (PFTs), including 10 vegetated types and 3 non-vegetated types (lake, land-ice, bare ground). For land-ice, CABLE does not allow fractional amount such that relevant grid cells must be all permanent ice, effectively limiting these cells to Greenland and Antarctica. CABLE calculates gross primary production (GPP) and leaf respiration at every time step using a two-leaf canopy scheme (Wang and Leuning, 1998) as a function of the leaf area index (LAI). LAI is calculated prognostically based on the size of the leaf carbon pool and the specific leaf area. Here the PFT is fixed such that vegetation is static, but LAI is interactive.

Biases in the ACCESS-ESM1.5 are discussed in Ziehn et al. (2020). In boreal summer, India and North America show signs of a warm bias, with a dry bias over India. In austral summer, there are warm biases over the equatorial regions in South America and Africa. By comparison, Australia's biases in temperature and precipitation are very small.

2.2 Experimental design

The Last Interglacial is one of the two interglacial periods included in PMIP4. The equilibrium experiment of the Last Inter-glacial, denoted lig127k, is classified as a Tier 1 PMIP4-CMIP6 experiment.

The initial conditions of the lig127k experiment were derived from a preindustrial simulation (1850 CE, piControl) (Ziehn et al., 2020), which follows the CMIP6 protocol (Eyring et al., 2016). piControl was integrated for 1000 years, and the average of the last 100 years serves as a reference to which the lig127k experiment is compared.

The lig127k experiment follows the lig127k protocol (Table 1, Otto-Bliesner et al. (2017)), with specific forcing values described in Table 1. As the solar constant in the piControl experiment follows CMIP5-PMIP3 guidelines (1365.65 W m^{-2}), it has a slightly different value to CMIP6 protocol (1360.75 W m^{-2}). The solar constant in lig127k is set equal to the one in piControl to allow a direct comparison between them. The experiment is integrated for 650 years, and we are presenting the last 200 years of that run. During the last 100 years, changes in globally averaged SST are +0.11 °C, changes in deep ocean temperature are +0.043 °C and changes in salinity in the Southern Ocean are less than 0.005 psu, which suggests that our experiment has equilibrated sufficiently.

Since the orbital parameters of LIG and PI are different (Table 1), a fixed-angular definition of months is required to achieve a valid comparison between lig127k, piControl, and proxy data. The length of each month should be defined by a fixed number of degrees of the Earth's orbit, as opposed to number of days. Therefore, the outputs of lig127k are adjusted following Bartlein and Shafer (2019). It is essential to consider this paleo-calendar effect for a correct interpretation of results.

3 Results

As the maximum insolation anomalies between the LIG and PI occur in June (+70 W m^{-2} at 80° N) and December (−45 W m^{-2} at 40° S) (Fig. 1), we here focus on climatic changes occurring in JJA and DJF.

3.1 Changes in surface temperature and sea-ice

Due to the large insolation anomalies in the NH during boreal summer (Fig. 1), simulated mean JJA surface air temperatures are 2.3 °C higher in the NH at the LIG compared to PI (Fig. 2b), in agreement with terrestrial proxy reconstructions from the region (Axford et al., 2011; Francis et al., 2006; Fréchette et al., 2006; McFarlin et al., 2018; Melles et al., 2012; Plikk et al., 2019; Salonen et al., 2018). The simulated boreal summer warming is maximum between 40° N and 60° N, averaging +6.5 °C over land, in line with the PMIP4 lig127k multi-model mean (Otto-Bliesner et al., 2021). Similarly, compared to the PI simulation, boreal summer SSTs are ∼2.5 °C higher in the North Pacific, the North Atlantic and the Nordic Seas, and up to 4 °C higher in the Labrador Sea (Fig. 2d). This high latitude warming is associated with a reduction in boreal summer Arctic sea-ice area (Fig. 2d), with a maximum of 63 % reduction in sea-ice area in September (Fig. S1, S2). North of 40° N in the North Atlantic and Norwegian Sea, 16 paleoproxy records suggest higher SSTs during boreal summer at the LIG and 9 suggest lower SSTs, with a range of −8.7°C to +5.7 °C, and a median of +1.5 °C (Fig. 2d). Out of these 25 records, simulated SSTs

4

agree with the anomaly sign of 16 of the paleoproxy records. The main regions of model-data disagreement, where proxy records suggest a cooling whereas the model suggests a warming, are in the Norwegian Sea and off the Iberian margin.

Due to the strong sea-ice melting in boreal summer, the simulated boreal winter Arctic sea-ice area remains 8 % smaller at the LIG compared to PI in spite of a higher rate of boreal autumn sea-ice formation (Fig. 2c, S1). In addition, enhanced deep water formation is simulated in the Labrador Sea during the LIG (not shown), inducing a $\sim$2.5 °C increase in winter SSTs in that region (Fig. 2c). However, paleoproxy records suggest there was no deep-water formation in the Labrador Sea during the LIG (Hillaire-Marcel et al., 2001) and the simulated SST increase in the Labrador Sea during JJA is in contrast with some of the SST paleoproxy records in that region (Fig. 2d; Capron et al., 2014, 2017). There is evidence of meltwater discharge from the Greenland ice-sheet during the early part of the LIG (Galaasen et al., 2014, 2020; Tzedakis et al., 2018), which could have suppressed deep ocean convection in the Labrador Sea and led to a cooling there (e.g. Tzedakis et al., 2018), thus explaining the discrepancy.

The simulated strength of the Atlantic Meridional Overturning Circulation (AMOC), as represented by the maximum meridional stream function at 26 °N in the Atlantic basin, is stronger at the LIG (21.8 Sv) than during PI (18.3 Sv). The AMOC strengthening and reduced Arctic sea-ice cover lead to $\sim$3°C higher winter SSTs in the northern North Atlantic and air surface temperatures over the ocean at high northern latitudes (+3.3 °C in 60–90° N) (Fig. 2a, c). Together with stronger NH insolation, the annual mean NH (0–90° N) surface air temperature is 1.4 °C higher at the LIG compared to PI (Fig. 3b).

Due to the lower magnitude of insolation in austral summer, simulated DJF SH air temperatures are lower at mid and low latitudes during the LIG compared to PI. This cooling is enhanced over land, where the anomalies can be as low as −5.4 °C in India (Fig. 2a). SSTs between 40° N and 40° S also drop by 0.5 °C on average during DJF, in good agreement with most proxy records in mid-latitudes. The largest SST drop at low-latitudes is simulated in the Bay of Bengal, with an anomaly of −3 °C (Fig. 2c). A $\sim$2 °C SST decrease is also simulated in the western equatorial Pacific and in the equatorial Atlantic. However, despite lower austral summer insolation at high southern latitudes, warmer conditions are simulated in DJF at the LIG compared to PI in the Southern Ocean, associated with a large decrease in sea-ice area (−43 %) (Fig. 2a, 2c and S1).

Compared to PI, the LIG insolation reaching 60° S is only 5 to 15 W m^{-2} larger between mid-April and mid-September (Fig. 1). However, this relatively small positive insolation anomaly reduces the growth of Antarctic sea-ice between April and September, with the simulated maximum Antarctic sea-ice area in September being 31 % smaller during the LIG than during PI (Fig. S1). Despite lower insolation, Antarctic sea-ice area reaches a minimum in February that is 46 % smaller at the LIG than at PI. This prominent reduction in Antarctic sea-ice area is accompanied by a marked temperature increase in the Southern Ocean all year round (Fig. 2). Simulated SSTs are 2 to 3 °C higher in the Southern Ocean during austral summer (Fig. 2d), while annual mean air temperatures over Antarctica increase close to the coast by $\sim$4 °C (Fig. 3b). The simulated Southern Ocean warming between 50° S and 60° S is in agreement with SST proxy records, however it is underestimated between $\sim$40° S and 50° S (Capron et al., 2017) (Fig. 2c). While the simulated warming is mostly confined to the south of 45° S, proxy records suggest the warming could have reached further north, particularly in the Atlantic Ocean. The differences in seasonal insolation makes the SH annual mean surface temperature 0.5 °C warmer in the LIG compared to PI, with a higher mean warming of 1.3 °C when averaged south of 50° S (Fig. 3b).

3.2 Precipitation change

Simulated annual mean precipitation anomalies are shown in Figure 3a, and compared to a recent compilation of LIG precipitation reconstructions based on a range of proxy records (including pollen, speleothems, landscape features, loess and sediment composition) (Scussolini et al., 2019). In the NH the model is in agreement with 64 out of 109 proxy records (59 %), i.e. where the model and proxy data show the same sign of change, or where the change in the simulations is <100 mm yr^{-1} and the corresponding proxy suggests no change. Although the agreement is not compellingly strong, it is worth pointing out that the majority of disagreements arises in central Europe where reconstructions are abundant and mostly display wetter conditions, whereas the simulation shows a slight decrease in precipitation. In contrast, there is a good model-data agreement in northern Africa, the Middle East, Asia and North America.

As seen in Figure 3a, the largest changes in annual mean precipitation are simulated in the tropics where both the rainfall mean and variability are higher. Annual precipitation increases over land in the northern tropics, particularly over the African Sahel (>+300 %), South Asia (+100 %), and Central America (+40 %). Coinciding with increasing precipitation, the significant cooling (~ -3 °C; Fig. 3b) over the Sahel and India is associated with stronger evaporation over land during boreal summer (not shown). All ocean regions in the northern tropics are simulated to be wetter, except for the South China Sea and Philippine Sea. In general there is good agreement with proxy records in the northern tropics.

In contrast, the model generally simulates drier conditions over the southern tropics during the LIG (Fig. 3a), particularly over South America (-20 %), South Africa (-40 %) and northern Australia (-40 %). This decrease in precipitation mostly occurs in DJF, during the SH monsoon season (Fig. 4c). In addition, this precipitation reduction is consistent with an overall increase in mean sea-level pressure over the SH land (Fig. 4f). Therefore, the simulation suggests a major change in precipitation in the tropics, associated with a shift in the Inter-Tropical Convergence Zone (ITCZ) and a weakening of the convergence zones in the SH, which will be discussed in the next section.

3.2.1 ITCZ changes

The ITCZ position is generally identified as the latitudinal band of maximum precipitation. Previous studies have demonstrated that the position of the ITCZ aligns with the zero energy flux equator, i.e. where the atmospheric meridional energy flux divergence vanishes (Schneider et al., 2014; Ceppi et al., 2013). In the present climate, this occurs north of the equator, thus placing the ITCZ in the NH. This is essentially due to an interhemispheric energy imbalance, caused primarily by the northward oceanic heat transport by the Atlantic Meridional Overturning Circulation (AMOC). The net northward oceanic heat transport to the NH is compensated by a southward atmospheric heat transport via a northward-displaced Hadley cell and the positioning of the ITCZ north of the Equator. Therefore, one would expect that an interhemispheric temperature gradient would drive a cross-equatorial atmospheric energy flux, which in turn determines the position of the ITCZ towards the warmer hemisphere (e.g., Schneider et al., 2014).

As seen in Figure 5h, zonally averaged precipitation in JJA displays a slight northward shift of the ITCZ at the LIG compared to PI. Although this northward ITCZ shift is seen in all ocean basins, there are differences in the magnitude of the peak

precipitation. The peak is 9 % stronger in the Pacific sector (130° E to 70° W), but 39 % weaker in the Atlantic sector. In the Indian sector (0 to 130° E), even though the ITCZ location is less defined, precipitation is higher between 5° S and 20° N at the LIG. In short, the ITCZ shifts northward in the Pacific and Atlantic sectors in JJA compared to PI. This consistent northward shift during JJA can be explained by the higher NH summer temperatures, which accentuate the interhemispheric temperature gradient.

The zonally averaged precipitation in DJF shows a more complex picture for the ITCZ, with an increase in strength (by 10 %) at 5° S, while precipitation at 5° N decreases by 23 % (Fig. 5d). However, the DJF precipitation response across basins varies significantly. In the Indian sector, there is a southward shift (∼3°) and slight strengthening of the ITCZ. In contrast, in the Pacific sector, which displays a double ITCZ in DJF in both PI and LIG, there is a weakening and northward shift (∼1° to 4°) of the precipitation peaks at 10° S and 7° N. Similarly, in the Atlantic sector, a ∼25 % weakening of DJF precipitation at 5° N during the LIG is simulated, while there is a strengthening of the ITCZ peaks at 5° S (Fig. 4a – c, 5c). The simulation thus displays a southward ITCZ shift over the Atlantic and Indian Oceans, but a northward shift in the Pacific Ocean. These differences in longitudinal responses are associated with changes in large-scale atmospheric circulation. Since low latitude precipitation is associated with monsoon systems, we will now look into more detail at the precipitation changes occurring in each of the monsoon regions.

3.2.2 Precipitation changes in monsoon regions

Monsoon domains are defined as regions in which the precipitation during the monsoon season is (1) greater than the dry season by at least 2.5 mm day^{-1}, and (2) responsible for at least 55% of the annual precipitation (Wang et al., 2011). For the NH, May-to-September is used as the monsoon wet season while November-to-March is the dry season. The reverse is adopted for the SH, i.e. November-to-March is the wet season, while the May-to-September is the dry season. As shown in Figure 6a, the model simulates a general expansion of the monsoon domains in the northern tropics, also associated with increased precipitation rates, whereas there is a contraction of the monsoon domains and reduced precipitation in the southern tropics.

The North African monsoon domain expands significantly into the Sahara region. This expansion is associated with enhanced southwesterly winds. The Indian monsoon also strengthens and expands due to intensified onshore winds from the Arabian Sea and convergence inland (Fig. 6a). On the other hand, a contraction of the monsoon domain over the Philippine Sea and South China Sea is simulated and attributed to a northeastern wind anomaly associated with trade winds strengthening in MJJAS.

As evident from Figure 6b, there is a marked difference in NDJFM precipitation anomalies over the SH land and ocean regions during LIG relative to PI. To investigate this difference further, we separate the simulated tropical precipitation anomalies over land and ocean (Fig. 7). The metrics on Fig. 7 have been calculated using an adjusted paleo-calendar from monthly outputs (Bartlein and Shafer, 2019). However, Brierley et al. (2020) suggest that this method might accentuate the anomalies. As seen in Fig. S3, non-calendar adjusted results are similar to the calendar adjusted ones (differences ∼<5 %), even though the calendar-adjusted results are slightly dry-biased for most precipitation-related metrics. The major difference is the total

precipitated water for the North African monsoon (NAF), in which the calendar adjusted suggest a ∼72 % increase, whereas the non-calendar adjusted suggest a ∼90 % increase.

225   Precipitation over land is generally higher in the northern tropics, with an increase of over 60 % in total precipitated water for the NAF (Fig. 7). The South Asian Monsoon (SA) also displays a large increase in precipitated water (>60 %), mainly due to a large increase in areal extent (+>55 %), as the increase in area-averaged precipitation is small (∼5 %). The North American monsoon (NAM) is slightly weaker, with a slight decrease in area-averaged precipitation rate (−0.3 %), areal extent (−2.2 %) and total precipitated water (−2.5 %). Compared to PI, all NH monsoon domains during the LIG experience an increase in air

230 surface temperature during monsoon seasons. While there is significant cooling during JJA over the Sahel at ∼15 °N and India due to stronger evaporation over land (Fig. 2b), this is compensated by the warming in higher latitudes.

    The contrary is simulated in the SH, with higher precipitation simulated over the ocean and lower precipitation, by at least 10 %, over land in the SH monsoon regions at the LIG compared to PI (Fig. 6b and 7). In the Indo-Australian region, there is a northward shift and weakening of the South Pacific Convergence Zone (SPCZ). This leads to a precipitation increase over the

235 western equatorial Pacific. Precipitation also increases at the southeastern edge of the SPCZ (Fig. 4c, 6b). This is linked to the weakening of the south Pacific high (Fig. 4f) and the associated westerlies south of 40 °S and the easterlies between 15 °S and 35 °S (Fig. 6b). The Australian monsoon (AUS) displays the greatest decline, with a decrease in total precipitated water over land by over 70 %, and a ∼60 % decrease in areal extent as the monsoon domain contracts northward. Drier conditions (<−1 mm day^{-1}) are also simulated over eastern Australia, even though it is not being included in the monsoon domain.

240   In contrast, the Indian Ocean Convergence Zone (IOCZ) shifts southward, which leads to a ∼8 % intensification of precipitation in the Indian Ocean between 10° S and 20° S, associated with a strengthening of northwesterly surface wind north of the IOCZ (Fig. 6b and 7). This southward shift is associated with an IOCZ weakening, which induces a 35 % decrease in total monsoonal precipitation over land in the South African monsoon region (SAF), and a 15 % decrease in the areal extent of the SAF. Central southern Africa (30° E, 15° S) displays the greatest decrease in summer precipitation. The monsoon domain

245 contracts along the north-south direction, but expands westward close to the equator on the west coast (15° E, 5° S). This could be linked to the southward shift of the ITCZ in the southern tropical Atlantic Ocean (Fig. 6b).

    Area-averaged precipitation associated with the South American monsoon (SAM) decreases by 21 % (Fig. 7), while the areal extent only decreases slightly as the monsoon domain remains spatially very similar to the PI (Fig. 6b). This means that the monsoon reduction is primarily due to weaker precipitation over the same region, with drier conditions more prevalent over

250 the west coast and the southern boundary of the monsoon domain (25° S), suggesting a weakening of the South Atlantic Convergence Zone (SACZ; Carvalho et al., 2002). The Brazilian coast along 0 to 15° S shows an increase in summer precipitation (+1 to +3 mm day^{-1}) due to the southward shift of the ITCZ in the Atlantic Ocean, but this does not contribute much to the general monsoon activity since LIG rainfall levels remain low.

    To a first order, the reduced precipitation over land in the southern tropics can be explained by the consistently colder

255 conditions over land masses in SH low to mid- latitudes during austral summer (Fig. 2a). Due to reduced land-sea temperature gradients, colder conditions over land induce a weakening of the onshore winds (i.e. a weakening of the easterlies over Brazil,

South Africa, northeastern Australia, and reduced north-westerlies in northwestern Australia), which tends to decrease moisture advection inland, and restrict convective activity over the SH land regions.

Due to the high heat capacity of the ocean, land masses are more sensitive to changes in insolation. As insolation is lower across most latitudes at the LIG compared to PI during austral summer, the strongest anomalous cooling occurs over land (Fig. 2a), which leads to positive surface pressure anomalies (Fig. 4f). In particular, the strong cooling over southwestern Australia (Fig. 2a) is associated with an anomalously high surface pressure (Fig. 4f), blocking the monsoonal inflow. The situation is similar in India: the strongest cooling occurs over the region centered on India, which induces positive pressure anomalies over the region and the northern part of the Indian Ocean. On the other hand, negative pressure anomalies develop in the southern tropical Indian Ocean. As a result the IOCZ shifts southward.

While the reduced insolation in the SH during DJF would tend to reduce precipitation over the SH, changes in the global atmospheric circulation produce a southward shift of the ITCZ in the Indian and Atlantic Oceans (Sect. 3.2.1, Fig. 4c, 5a, and 5c) that leads to higher precipitation over those tropical ocean regions (Fig. 7). In addition, the land-ocean contrast helps maintain this configuration via changes in zonal pressure gradient between land and adjacent oceans, creating local Walker-type circulation anomalies (with anomalous ascending motion over oceans and compensatory subsidence over land).

A strengthening of the Hadley circulation in the SH is simulated in DJF (Fig. 8). It contributes to the simulated drier conditions in the subtropics at ∼30° S due to greater subsidence, as seen from the increase of surface pressures over land. The southern boundary of the Hadley cell also experiences a slight northward shift, from ∼36° S to ∼33° S (see the zero contour in Fig. 8), which pushes regions of high pressure in the subtropics to the north (Fig. 4f). This favours an anomalous subsidence and weaker convection over the SH convergence zones thus reducing monsoonal precipitation.

4   Discussion

At the LIG the insolation reaching Earth was different from PI, with higher insolation in JJA in the NH and lower insolation in DJF in the SH. In agreement with paleo-records, the ACCESS-ESM1.5 lig127k simulation presented here suggests a 2 to 4 °C SST increase in the North Atlantic as well as a 5 °C warming over land in the mid-northern latitudes in JJA. The simulated northern latitude temperature anomalies as well as JJA Arctic sea-ice cover are very close to the PMIP4 lig127k multi-model means (Kageyama et al., 2021; Otto-Bliesner et al., 2021). The simulated Arctic LIG sea-ice cover is in agreement with 16 out of 27 proxy records, and suggests that the simulated LIG Arctic sea-ice cover might be slightly overestimated (Kageyama et al., 2021).

At low to mid southern latitudes, simulated surface air temperature anomalies in the ACCESS-ESM are also very similar to the PMIP4 multi-model mean with ∼3 °C warming over land in JJA, and ∼2 °C cooling over land in DJF. However, the model simulates much warmer conditions over the Southern Ocean all year round, with values higher than the multi-model mean. This is concurrent with a large decrease in Southern Ocean sea-ice at the LIG. While the simulated warming over the Southern Ocean throughout the year is at the higher end of the PMIP4 lig127k model range, the warming over Antarctica is at the lower end (Otto-Bliesner et al., 2021).

The simulated spatial distribution of annual precipitation anomalies (Fig. 3a) agrees well with the PMIP4 multi-model mean (Otto-Bliesner et al., 2021), with drier conditions over SH land regions including North Australia, South Africa and South America, while wetter conditions are simulated at ∼10° S in the Atlantic Ocean, the Indian Ocean and the western equatorial Pacific Ocean. However, while our simulation suggests wetter conditions over the equatorial Pacific at 10° N due to a strengthening of the ITCZ in this basin in JJA (Fig. 5f), this does not occur in the multi-model mean.

Reduced precipitation over land and increased precipitation over the ocean in DJF in low to mid-southern latitudes is also evident in the PMIP4 multi-model mean, indicating that the ACCESS-ESM1.5 lig127k simulation provides a good representation of the LIG features as simulated by coupled climate models. Despite the strong signal emanating from the lig127k simulations, these precipitation anomalies are not necessarily evident from SH paleoproxy records, highlighting the need for additional hydrological records from low- and mid- southern latitudes. Furthermore, the lig127k is an equilibrium simulation, which does not take into account potential meltwater discharges from the Antarctic and Greenland ice-sheets, and their associated impact on deep water formation and therefore variability in ocean and atmospheric circulation (e.g. Hayes et al., 2014; Rohling et al., 2019; Tzedakis et al., 2018). The time evolution across the LIG of the hydrological proxy records should thus be looked at in detail, and additional LIG experiments including North Atlantic and/or Southern Ocean meltwater pulses should be performed.

The orbital forcings and latitude-month insolation anomalies relative to PI are similar between the LIG and mid-Holocene (6 ka). SH monsoons are also weakened and contracted during the mid-Holocene (D'Agostino et al., 2020), with similar SH land-sea precipitation contrast patterns compared to lig127k. The reduced monsoonal precipitation in the mid-Holocene is largely attributed to changes in atmospheric mean flow (i.e. the Walker and Hadley circulations) and the decrease in net energy input (D'Agostino et al., 2020). While an energetic approach is beyond the scope of this study, the weakening of SH monsoons in our lig127k simulation are indeed associated with weaker local insolation during the wet season, which leads to reduced surface air temperature (Fig. 2a) and increased surface pressure over land (Fig. 4f). One can therefore hypothesise that the weakening of SH monsoons in lig127k might also be associated with a similar decrease in net energy input. Furthermore, as the changes in the Walker and Hadley cells are not analysed in detail here, a closer examination of the relationship between SH monsoons and these large-scale atmospheric circulations is recommended for future studies.

Additional studies looking into the details of the mechanisms leading to changes in the SH monsoon systems, and their relationship to low latitude modes of variability, such as the El Niño Southern Oscillation and the Indian Ocean Dipole, are needed. Under LIG conditions, these modes of variability might be altered in terms of magnitude and spatial variation, which might have contributed to changes in rainfall variability and, to a lesser extent, mean precipitation over the monsoon regions. Indeed a recent study shows that ENSO variability was shown to be consistently reduced during the LIG compared to PI, with the ensemble mean of PMIP4 simulations suggesting a 20 % weakening of ENSO amplitude (Brown et al., 2020a). To what extent an ENSO weakening may have contributed to mean state changes over the SH monsoon system is unclear and subject for future exploration.

A significant reduction in precipitation in the tropical regions of the SH would have impacted vegetation during the LIG. Changes in vegetation cover are not taken into account in our study, but the LAI was interactive in the model. The simulated change in LAI is consistent with precipitation. For example, the LAI is decreased during boreal summer and autumn at ∼50°

N across Eurasia and North America in regions with less summer rainfall during the LIG (Fig. S4). In contrast, increased precipitation over the Sahel and surrounding regions (Fig. 6a) corresponds to elevated LAI. This affects evapotranspiration, as an increase in LAI enhances canopy evapotranspiration, while reducing soil evaporation, and ultimately also alters the hydrological cycle.

It has been previously shown that due to changes in albedo and moisture availability, changes in vegetation might amplify the changes in precipitation (e.g. Messori et al., 2019). For example, a large increase in precipitation over the Sahel would lead to a greening of the Sahara (Hopcroft et al., 2017; Larrasoaña et al., 2013; Osborne et al., 2008; Pausata et al., 2020). The greening would tend to increase the sensible and latent heat fluxes into the atmosphere, and produce a cyclonic circulation anomaly over the Sahara, whose anomalous westerly flow would transport more moisture from the neighbouring Atlantic Ocean into the region (Messori et al., 2019; Patricola and Cook, 2007; Rachmayani et al., 2015). Additional simulations with interactive vegetation, or with prescribed changes in vegetation cover, should thus be performed to quantify the coupled effect of precipitation and vegetation changes.

Due to the importance of the SH monsoon systems for water availability, such reduced precipitation in the southern tropics in a past warmer world are concerning. However, since these negative precipitation anomalies mostly result from the strong cooling over land, such hydrological changes are not currently expected over the coming centuries under the RCP/SSP (Representative Concentration Pathway / Shared Socioeconomic Pathways) scenarios where future climate changes are due to greenhouse gas forcing and not to changes in orbital parameters. In fact, moisture budget analysis has shown that SH monsoon expands and intensifies under the RCP8.5 scenario (D'Agostino et al., 2020). Incidentally, lig127k shows increased precipitation at the southeastern edge of the SPCZ, which is associated with the weakening of the local high pressure region. Such enhanced moisture at the eastern SPCZ margin is also linked to a reduction in trade wind inflow from the southeastern Pacific (Fig. 6b), as previously demonstrated by Lintner and Neelin (2008). Interestingly, CMIP5 models project drier conditions over the southeastern edge of the SPCZ due to the transport of dry subtropical air into the region (Brown et al., 2020b), thus suggesting a different mechanism can take place in a warmer climate. CMIP6 future projections indeed generally simulate no significant changes in the Australian, South African and South American monsoons by 2100 under all SSP scenarios, while drier conditions are simulated over these regions in JJA (Cook et al., 2020). In Australia, northern rainfall in DJFMAM is more constrained in CMIP6 than in CMIP5 and it is projected to experience a ∼2 % increase by the year 2090 under high-emission scenario (RCP8.5 and SSP5-85; Grose et al., 2020), which is a small change compared to the decrease in our LIG simulation (Fig. 7).

In conclusion, drier conditions are simulated over SH land during austral summer in the lig127k experiment and all SH monsoons are found to be consistently weaker compared to PI. At the same time, summer precipitation over southern tropical oceans is higher, associated with a southward shift of the ITCZ in DJF in the Indian and Atlantic Oceans. The dry conditions are caused by reduced land-sea temperature contrast due to cooling over land, and also higher mean sea level pressure attributed from greater subsidence as the SH Hadley cell strengthens.

References

Axford, Y., Briner, J. P., Francis, D. R., Miller, G. H., Walker, I. R., and Wolfe, A. P.: Chironomids record terrestrial temperature changes throughout Arctic interglacials of the past 200,000 yr, GSA Bulletin, 123, 1275–1287, https://doi.org/10.1130/B30329.1, 2011.

Bartlein, P. J. and Shafer, S. L.: Paleo calendar-effect adjustments in time-slice and transient climate-model simulations (PaleoCalAdjust v1.0): impact and strategies for data analysis, Geoscientific Model Development, 12, 3889–3913, https://doi.org/10.5194/gmd-12-3889-2019, https://www.geosci-model-dev.net/12/3889/2019/, 2019.

Berger, A.: Long-Term Variations of Daily Insolation and Quaternary Climatic Changes, Journal of the Atmospheric Sciences, 35, 2362–2367, https://doi.org/10.1175/1520-0469(1978)035<2362:LTVODI>2.0.CO;2, 1978.

Bi, D., Dix, M., Marsland, S., O'Farrell, S., Rashid, H., Uotila, P., Hirst, A., Kowalczyk, E., Golebiewski, M., Sullivan, A., Yan, Y., Hannah, N., Franklin, C., Sun, Z., Vohralik, P., Watterson, I., Zhou, K., Fiedler, R., Collier, M., and Puri, K.: The ACCESS coupled model: Description, control climate and evaluation, Australian Meteorological and Oceanographic Journal, 63, 41–64, https://doi.org/10.22499/2.6301.004, 2012.

Brierley, C. M., Zhao, A., Harrison, S. P., Braconnot, P., Williams, C. J. R., Thornalley, D. J. R., Shi, X., Peterschmitt, J.-Y., Ohgaito, R., Kaufman, D. S., Kageyama, M., Hargreaves, J. C., Erb, M. P., Emile-Geay, J., D'Agostino, R., Chandan, D., Carré, M., Bartlein, P. J., Zheng, W., Zhang, Z., Zhang, Q., Yang, H., Volodin, E. M., Tomas, R. A., Routson, C., Peltier, W. R., Otto-Bliesner, B., Morozova, P. A., McKay, N. P., Lohmann, G., Legrande, A. N., Guo, C., Cao, J., Brady, E., Annan, J. D., and Abe-Ouchi, A.: Large-scale features and evaluation of the PMIP4-CMIP6 *midHolocene* simulations, Climate of the Past, 16, 1847–1872, https://doi.org/10.5194/cp-16-1847-2020, https://cp.copernicus.org/articles/16/1847/2020/, 2020.

Brown, J. R., Brierley, C. M., An, S.-I., Guarino, M.-V., Stevenson, S., Williams, C. J. R., Zhang, Q., Zhao, A., Abe-Ouchi, A., Braconnot, P., Brady, E. C., Chandan, D., D'Agostino, R., Guo, C., LeGrande, A. N., Lohmann, G., Morozova, P. A., Ohgaito, R., O'ishi, R., Otto-Bliesner, B. L., Peltier, W. R., Shi, X., Sime, L., Volodin, E. M., Zhang, Z., and Zheng, W.: Comparison of past and future simulations of ENSO in CMIP5/PMIP3 and CMIP6/PMIP4 models, Climate of the Past, 16, 1777–1805, https://doi.org/10.5194/cp-16-1777-2020, https://cp.copernicus.org/articles/16/1777/2020/, 2020a.

Brown, J. R., Lengaigne, M., Lintner, B. R., Widlansky, M. J., van der Wiel, K., Dutheil, C., Linsley, B. K., Matthews, A. J., and Renwick, J.: South Pacific Convergence Zone dynamics, variability and impacts in a changing climate, Nature Reviews Earth & Environment, 1, 530–543, https://doi.org/10.1038/s43017-020-0078-2, 2020b.

CAPE-Last Interglacial Project Members: Last Interglacial Arctic warmth confirms polar amplification of climate change, Quaternary Science Reviews, 25, 1383–1400, https://doi.org/10.1016/j.quascirev.2006.01.033, http://www.sciencedirect.com/science/article/pii/S0277379106000990, 2006.

Capron, E., Govin, A., Stone, E. J., Masson-Delmotte, V., Mulitza, S., Otto-Bliesner, B., Rasmussen, T. L., Sime, L. C., Waelbroeck, C., and Wolff, E. W.: Temporal and spatial structure of multi-millennial temperature changes at high latitudes during the Last Interglacial, Quaternary Science Reviews, 103, 116–133, https://doi.org/10.1016/j.quascirev.2014.08.018, http://www.sciencedirect.com/science/article/pii/S0277379114003382, 2014.

Capron, E., Govin, A., Feng, R., Otto-Bliesner, B., and Wolff, E.: Critical evaluation of climate syntheses to benchmark CMIP6/PMIP4 127 ka Last Interglacial simulations in the high-latitude regions, Quaternary Science Reviews, 168, 137–150, https://doi.org/10.1016/j.quascirev.2017.04.019, http://www.sciencedirect.com/science/article/pii/S0277379117303487, 2017.

Carvalho, L. M. V., Jones, C., and Liebmann, B.: Extreme Precipitation Events in Southeastern South America and Large-Scale Convective Patterns in the South Atlantic Convergence Zone, Journal of Climate, 15, 2377–2394, 2002.

405 Ceppi, P., Hwang, Y.-T., Liu, X., Frierson, D. M. W., and Hartmann, D. L.: The relationship between the ITCZ and the Southern Hemispheric eddy-driven jet, Journal of Geophysical Research: Atmospheres, 118, 5136–5146, https://doi.org/10.1002/jgrd.50461, 2013.

Cook, B. I., Mankin, J. S., Marvel, K., Williams, A. P., Smerdon, J. E., and Anchukaitis, K. J.: Twenty-First Century Drought Projections in the CMIP6 Forcing Scenarios, Earth's Future, 8, e2019EF001 461, https://doi.org/10.1029/2019EF001461, https://agupubs.onlinelibrary.wiley.com/doi/abs/10.1029/2019EF001461, 2020.

410 D'Agostino, R., Brown, J. R., Moise, A., Nguyen, H., Dias, P. L. S., and Jungclaus, J.: Contrasting Southern Hemisphere Monsoon Response: MidHolocene Orbital Forcing versus Future Greenhouse Gas–Induced Global Warming, Journal of Climate, 33, 9595–9613, https://doi.org/10.1175/JCLI-D-19-0672.1, https://journals.ametsoc.org/view/journals/clim/33/22/jcliD190672.xml, 2020.

Dutton, A. and Lambeck, K.: Ice Volume and Sea Level During the Last Interglacial, Science, 337, 216–219, https://doi.org/10.1126/science.1205749, https://science.sciencemag.org/content/337/6091/216, 2012.

415 Dutton, A., Carlson, A. E., Long, A. J., Milne, G. A., Clark, P. U., DeConto, R., Horton, B. P., Rahmstorf, S., and Raymo, M. E.: Sea-level rise due to polar ice-sheet mass loss during past warm periods, Science, 349, https://doi.org/10.1126/science.aaa4019, https://science.sciencemag.org/content/349/6244/aaa4019, 2015.

Eyring, V., Bony, S., Meehl, G. A., Senior, C. A., Stevens, B., Stouffer, R. J., and Taylor, K. E.: Overview of the Coupled Model Intercomparison Project Phase 6 (CMIP6) experimental design and organization, Geoscientific Model Development, 9, 1937–1958,
420 https://doi.org/10.5194/gmd-9-1937-2016, https://www.geosci-model-dev.net/9/1937/2016/, 2016.

Francis, D. R., Wolfe, A. P., Walker, I. R., and Miller, G. H.: Interglacial and Holocene temperature reconstructions based on midge remains in sediments of two lakes from Baffin Island, Nunavut, Arctic Canada, Palaeogeography, Palaeoclimatology, Palaeoecology, 236, 107–124, https://doi.org/10.1016/j.palaeo.2006.01.005, http://www.sciencedirect.com/science/article/pii/S0031018206000277, 2006.

Fréchette, B., Wolfe, A. P., Miller, G. H., Richard, P. J. H., and de Vernal, A.: Vegetation and climate of the last interglacial on Baffin
425 Island, Arctic Canada, Palaeogeography, Palaeoclimatology, Palaeoecology, 236, 91–106, https://doi.org/10.1016/j.palaeo.2005.11.034, http://www.sciencedirect.com/science/article/pii/S0031018206001349, 2006.

Galaasen, E. V., Ninnemann, U. S., Irvalı, N., Kleiven, H. K. F., Rosenthal, Y., Kissel, C., and Hodell, D. A.: Rapid Reductions in North Atlantic Deep Water During the Peak of the Last Interglacial Period, Science, 343, 1129–1132, https://doi.org/10.1126/science.1248667, https://science.sciencemag.org/content/343/6175/1129, 2014.

430 Galaasen, E. V., Ninnemann, U. S., Kessler, A., Irvalı, N., Rosenthal, Y., Tjiputra, J., Bouttes, N., Roche, D. M., Kleiven, H. K. F., and Hodell, D. A.: Interglacial instability of North Atlantic Deep Water ventilation, Science, 367, 1485–1489, https://doi.org/10.1126/science.aay6381, https://science.sciencemag.org/content/367/6485/1485, 2020.

Griffies, S. M.: Elements of the Modular Ocean Model (MOM) 5 (2012 release with updates), Technical Report 7, Tech. rep., NOAA/Geophysical Fluid Dynamics Laboratory Ocean Group, 2014.

435 Grose, M. R., Narsey, S., Delage, F. P., Dowdy, A. J., Bador, M., Boschat, G., Chung, C., Kajtar, J. B., Rauniyar, S., Freund, M. B., Lyu, K., Rashid, H., Zhang, X., Wales, S., Trenham, C., Holbrook, N. J., Cowan, T., Alexander, L., Arblaster, J. M., and Power, S.: Insights From CMIP6 for Australia's Future Climate, Earth's Future, 8, e2019EF001 469, https://doi.org/10.1029/2019EF001469, https://agupubs.onlinelibrary.wiley.com/doi/abs/10.1029/2019EF001469, 2020.

Hayes, C. T., Martínez-García, A., Hasenfratz, A. P., Jaccard, S. L., Hodell, D. A., Sigman, D. M., Haug, G. H., and Anderson, R. F.: A stagnation event in the deep South Atlantic during the last interglacial period, Science, 346, 1514–1517, https://doi.org/10.1126/science.1256620, https://science.sciencemag.org/content/346/6216/1514, 2014.

Hoffman, J. S., Clark, P. U., Parnell, A. C., and He, F.: Regional and global sea-surface temperatures during the last interglaciation, Science, 355, 276–279, https://doi.org/10.1126/science.aai8464, https://science.sciencemag.org/content/355/6322/276, 2017.

Hopcroft, P. O., Valdes, P. J., Harper, A. B., and Beerling, D. J.: Multi vegetation model evaluation of the Green Sahara climate regime, Geophysical Research Letters, 44, 6804–6813, https://doi.org/10.1002/2017GL073740, 2017.

Hunke, E. C. and Lipscomb, W. H.: CICE: The Los Alamos Sea Ice Model. Documentation and software user's manual version 4.1, Tech. Rep. LA-CC-06-012, Tech. rep., T-3 Fluid Dyn. Group, Los Alamos Natl. Lab., Los Alamos, N. M., 2010.

Kageyama, M., Sime, L. C., Sicard, M., Guarino, M.-V., de Vernal, A., Stein, R., Schroeder, D., Malmierca-Vallet, I., Abe-Ouchi, A., Bitz, C., Braconnot, P., Brady, E. C., Cao, J., Chamberlain, M. A., Feltham, D., Guo, C., LeGrande, A. N., Lohmann, G., Meissner, K. J., Menviel, L., Morozova, P., Nisancioglu, K. H., Otto-Bliesner, B. L., O'ishi, R., Ramos Buarque, S., Salas y Melia, D., Sherriff-Tadano, S., Stroeve, J., Shi, X., Sun, B., Tomas, R. A., Volodin, E., Yeung, N. K. H., Zhang, Q., Zhang, Z., Zheng, W., and Ziehn, T.: A multi-model CMIP6-PMIP4 study of Arctic sea ice at 127 ka: sea ice data compilation and model differences, Climate of the Past, 17, 37–62, https://doi.org/10.5194/cp-17-37-2021, https://cp.copernicus.org/articles/17/37/2021/, 2021.

Kopp, R. E., Simons, F. J., Mitrovica, J. X., Maloof, A. C., and Oppenheimer, M.: Probabilistic assessment of sea level during the last interglacial stage, Nature, 462, 863–867, https://doi.org/10.1038/nature08686, 2009.

Kowalczyk, E., Stevens, Law, Dix, M., Wang, Y., Harman, I., Haynes, Srbinovsky, Pak, B., and Ziehn, T.: The land surface model component of ACCESS: Description and impact on the simulated surface climatology, Australian Meteorological and Oceanographic Journal, AMOJ, 65–82, 2013.

Landais, A., Masson-Delmotte, V., Capron, E., Langebroek, P. M., Bakker, P., Stone, E. J., Merz, N., Raible, C. C., Fischer, H., Orsi, A., Prié, F., Vinther, B., and Dahl-Jensen, D.: How warm was Greenland during the last interglacial period?, Climate of the Past, 12, 1933–1948, https://doi.org/10.5194/cp-12-1933-2016, https://www.clim-past.net/12/1933/2016/, 2016.

Larrasoaña, J. C., Roberts, A. P., and Rohling, E. J.: Dynamics of green Sahara periods and their role in hominin evolution, PloS one, 8, e76 514–e76 514, https://doi.org/10.1371/journal.pone.0076514, https://pubmed.ncbi.nlm.nih.gov/24146882, 2013.

Law, R. M., Ziehn, T., Matear, R. J., Lenton, A., Chamberlain, M. A., Stevens, L. E., Wang, Y.-P., Srbinovsky, J., Bi, D., Yan, H., and Vohralik, P. F.: The carbon cycle in the Australian Community Climate and Earth System Simulator (ACCESS-ESM1) – Part 1: Model description and pre-industrial simulation, Geoscientific Model Development, 10, 2567–2590, https://doi.org/10.5194/gmd-10-2567-2017, https://www.geosci-model-dev.net/10/2567/2017/, 2017.

Lintner, B. R. and Neelin, J. D.: Eastern margin variability of the South Pacific Convergence Zone, Geophysical Research Letters, 35, https://doi.org/10.1029/2008GL034298, 2008.

Magiera, M., Lechleitner, F. A., Erhardt, A. M., Hartland, A., Kwiecien, O., Cheng, H., Bradbury, H. J., Turchyn, A. V., Riechelmann, S., Edwards, L., and Breitenbach, S. F. M.: Local and Regional Indian Summer Monsoon Precipitation Dynamics During Termination II and the Last Interglacial, Geophysical Research Letters, 46, 12 454–12 463, https://doi.org/10.1029/2019GL083721, https://agupubs.onlinelibrary.wiley.com/doi/abs/10.1029/2019GL083721, 2019.

Martin, G. M., Milton, S. F., Senior, C. A., Brooks, M. E., Ineson, S., Reichler, T., and Kim, J.: Analysis and Reduction of Systematic Errors through a Seamless Approach to Modeling Weather and Climate, Journal of Climate, 23, 5933–5957, https://doi.org/10.1175/2010JCLI3541.1, 2010.

Masson-Delmotte, V., Schulz, M., Abe-Ouchi, A., Beer, J., Ganopolski, A., Rouco, J. G., Jansen, E., Lambeck, K., Luterbacher, J., Naish, T., et al.: Information from Paleoclimate Archives In: Climate Change 2013: The Physical Science Basis Contribution of Working Group I to the Fifth Assessment Report of the Intergovernmental Panel on Climate Change ed TF Stocker et al, Cambridge, United Kingdom and New York, NY, USA, 2013.

McFarlin, J. M., Axford, Y., Osburn, M. R., Kelly, M. A., Osterberg, E. C., and Farnsworth, L. B.: Pronounced summer warming in northwest Greenland during the Holocene and Last Interglacial, Proceedings of the National Academy of Sciences, 115, 6357, https://doi.org/10.1073/pnas.1720420115, http://www.pnas.org/content/115/25/6357.abstract, 2018.

Melles, M., Brigham-Grette, J., Minyuk, P. S., Nowaczyk, N. R., Wennrich, V., DeConto, R. M., Anderson, P. M., Andreev, A. A., Coletti, A., Cook, T. L., Haltia-Hovi, E., Kukkonen, M., Lozhkin, A. V., Rosén, P., Tarasov, P., Vogel, H., and Wagner, B.: 2.8 Million Years of Arctic Climate Change from Lake El'gygytgyn, NE Russia, Science, 337, 315–320, https://doi.org/10.1126/science.1222135, https://science.sciencemag.org/content/337/6092/315, 2012.

Messori, G., Gaetani, M., Zhang, Q., Zhang, Q., and Pausata, F. S. R.: The water cycle of the mid-Holocene West African monsoon: The role of vegetation and dust emission changes, International Journal of Climatology, 39, 1927–1939, https://doi.org/10.1002/joc.5924, https://rmets.onlinelibrary.wiley.com/doi/abs/10.1002/joc.5924, 2019.

NEEM community members, Dahl-Jensen, D., Albert, M. R., Aldahan, A., Azuma, N., Balslev-Clausen, D., Baumgartner, M., Berggren, A. M., Bigler, M., Binder, T., Blunier, T., Bourgeois, J. C., Brook, E. J., Buchardt, S. L., Buizert, C., Capron, E., Chappellaz, J., Chung, J., Clausen, H. B., Cvijanovic, I., Davies, S. M., Ditlevsen, P., Eicher, O., Fischer, H., Fisher, D. A., Fleet, L. G., Gfeller, G., Gkinis, V., Gogineni, S., Goto-Azuma, K., Grinsted, A., Gudlaugsdottir, H., Guillevic, M., Hansen, S. B., Hansson, M., Hirabayashi, M., Hong, S., Hur, S. D., Huybrechts, P., Hvidberg, C. S., Iizuka, Y., Jenk, T., Johnsen, S. J., Jones, T. R., Jouzel, J., Karlsson, N. B., Kawamura, K., Keegan, K., Kettner, E., Kipfstuhl, S., Kjær, H. A., Koutnik, M., Kuramoto, T., Köhler, P., Laepple, T., Landais, A., Langen, P. L., Larsen, L. B., Leuenberger, D., Leuenberger, M., Leuschen, C., Li, J., Lipenkov, V., Martinerie, P., Maselli, O. J., Masson-Delmotte, V., McConnell, J. R., Miller, H., Mini, O., Miyamoto, A., Montagnat-Rentier, M., Mulvaney, R., Muscheler, R., Orsi, A. J., Paden, J., Panton, C., Pattyn, F., Petit, J. R., Pol, K., Popp, T., Possnert, G., Prié, F., Prokopiou, M., Quiquet, A., Rasmussen, S. O., Raynaud, D., Ren, J., Reutenauer, C., Ritz, C., Röckmann, T., Rosen, J. L., Rubino, M., Rybak, O., Samyn, D., Sapart, C. J., Schilt, A., Schmidt, A. M. Z., Schwander, J., Schüpbach, S., Seierstad, I., Severinghaus, J. P., Sheldon, S., Simonsen, S. B., Sjolte, J., Solgaard, A. M., Sowers, T., Sperlich, P., Steen-Larsen, H. C., Steffen, K., Steffensen, J. P., Steinhage, D., Stocker, T. F., Stowasser, C., Sturevik, A. S., Sturges, W. T., Sveinbjörnsdottir, A., Svensson, A., Tison, J. L., Uetake, J., Vallelonga, P., van de Wal, R. S. W., van der Wel, G., Vaughn, B. H., Vinther, B., Waddington, E., Wegner, A., Weikusat, I., White, J. W. C., Wilhelms, F., Winstrup, M., Witrant, E., Wolff, E. W., Xiao, C., and Zheng, J.: Eemian interglacial reconstructed from a Greenland folded ice core, Nature, 493, https://doi.org/10.1038/nature11789, 2013.

Oke, P. R., Griffin, D. A., Schiller, A., Matear, R. J., Fiedler, R., Mansbridge, J., Lenton, A., Cahill, M., Chamberlain, M. A., and Ridgway, K.: Evaluation of a near-global eddy-resolving ocean model, Geoscientific Model Development, 6, 591–615, https://doi.org/10.5194/gmd-6-591-2013, https://www.geosci-model-dev.net/6/591/2013/, 2013.

Orland, I. J., He, F., Bar-Matthews, M., Chen, G., Ayalon, A., and Kutzbach, J. E.: Resolving seasonal rainfall changes in the Middle East during the last interglacial period, Proceedings of the National Academy of Sciences, 116, 24 985–24 990, https://doi.org/10.1073/pnas.1903139116, https://www.pnas.org/content/116/50/24985, 2019.

Osborne, A. H., Vance, D., Rohling, E. J., Barton, N., Rogerson, M., and Fello, N.: A humid corridor across the Sahara for the migration of early modern humans out of Africa 120,000 years ago, Proceedings of the National Academy of Sciences, 105, 16 444, https://doi.org/10.1073/pnas.0804472105, http://www.pnas.org/content/105/43/16444.abstract, 2008.

Otto-Bliesner, B. L., Braconnot, P., Harrison, S. P., Lunt, D. J., Abe-Ouchi, A., Albani, S., Bartlein, P. J., Capron, E., Carlson, A. E., Dutton, A., Fischer, H., Goelzer, H., Govin, A., Haywood, A., Joos, F., LeGrande, A. N., Lipscomb, W. H., Lohmann, G., Mahowald, N., Nehrbass-Ahles, C., Pausata, F. S. R., Peterschmitt, J.-Y., Phipps, S. J., Renssen, H., and Zhang, Q.: The PMIP4 contribution to CMIP6 – Part 2: Two interglacials, scientific objective and experimental design for Holocene and Last Interglacial simulations, Geoscientific Model Development, 10, 3979–4003, https://doi.org/10.5194/gmd-10-3979-2017, https://www.geosci-model-dev.net/10/3979/2017/, 2017.

Otto-Bliesner, B. L., Brady, E. C., Zhao, A., Brierley, C. M., Axford, Y., Capron, E., Govin, A., Hoffman, J. S., Isaacs, E., Kageyama, M., Scussolini, P., Tzedakis, P. C., Williams, C. J. R., Wolff, E., Abe-Ouchi, A., Braconnot, P., Ramos Buarque, S., Cao, J., de Vernal, A., Guarino, M. V., Guo, C., LeGrande, A. N., Lohmann, G., Meissner, K. J., Menviel, L., Morozova, P. A., Nisancioglu, K. H., O'ishi, R., Salas y Mélia, D., Shi, X., Sicard, M., Sime, L., Stepanek, C., Tomas, R., Volodin, E., Yeung, N. K. H., Zhang, Q., Zhang, Z., and Zheng, W.: Large-scale features of Last Interglacial climate: results from evaluating the *lig127k* simulations for the Coupled Model Intercomparison Project (CMIP6)–Paleoclimate Modeling Intercomparison Project (PMIP4), Climate of the Past, 17, 63–94, https://doi.org/10.5194/cp-17-63-2021, https://cp.copernicus.org/articles/17/63/2021/, 2021.

Patricola, C. M. and Cook, K. H.: Dynamics of the West African Monsoon under Mid-Holocene Precessional Forcing: Regional Climate Model Simulations, Journal of Climate, 20, 694–716, https://doi.org/10.1175/JCLI4013.1, 2007.

Pausata, F. S. R., Gaetani, M., Messori, G., Berg, A., Maia de Souza, D., Sage, R. F., and deMenocal, P. B.: The Greening of the Sahara: Past Changes and Future Implications, One Earth, 2, 235–250, https://doi.org/10.1016/j.oneear.2020.03.002, http://www.sciencedirect.com/science/article/pii/S2590332220301007, 2020.

Plikk, A., Engels, S., Luoto, T. P., Nazarova, L., Salonen, J. S., and Helmens, K. F.: Chironomid-based temperature reconstruction for the Eemian Interglacial (MIS 5e) at Sokli, northeast Finland, Journal of Paleolimnology, 61, 355–371, https://doi.org/10.1007/s10933-018-00064-y, 2019.

Rachmayani, R., Prange, M., and Schulz, M.: North African vegetation–precipitation feedback in early and mid-Holocene climate simulations with CCSM3-DGVM, Climate of the Past, 11, 175–185, https://doi.org/10.5194/cp-11-175-2015, https://cp.copernicus.org/articles/11/175/2015/, 2015.

Rohling, E., Cane, T., Cooke, S., Sprovieri, M., Bouloubassi, I., Emeis, K., Schiebel, R., Kroon, D., Jorissen, F., Lorre, A., and Kemp, A.: African monsoon variability during the previous interglacial maximum, Earth and Planetary Science Letters, 202, 61–75, https://doi.org/10.1016/S0012-821X(02)00775-6, http://www.sciencedirect.com/science/article/pii/S0012821X02007756, 2002.

Rohling, E. J., Hibbert, F. D., Grant, K. M., Galaasen, E. V., Irvalı, N., Kleiven, H. F., Marino, G., Ninnemann, U., Roberts, A. P., Rosenthal, Y., Schulz, H., Williams, F. H., and Yu, J.: Asynchronous Antarctic and Greenland ice-volume contributions to the last interglacial sea-level highstand, Nature Communications, 10, 5040, https://doi.org/10.1038/s41467-019-12874-3, 2019.

Salonen, J. S., Helmens, K. F., Brendryen, J., Kuosmanen, N., Väliranta, M., Goring, S., Korpela, M., Kylander, M., Philip, A., Plikk, A., Renssen, H., and Luoto, M.: Abrupt high-latitude climate events and decoupled seasonal trends during the Eemian, Nature Communications, 9, 2851, https://doi.org/10.1038/s41467-018-05314-1, 2018.

Schneider, T., Bischoff, T., and Haug, G. H.: Migrations and dynamics of the intertropical convergence zone, Nature, 513, 45–53, https://doi.org/10.1038/nature13636, 2014.

Scussolini, P., Bakker, P., Guo, C., Stepanek, C., Zhang, Q., Braconnot, P., Cao, J., Guarino, M.-V., Coumou, D., Prange, M., Ward, P. J., Renssen, H., Kageyama, M., Otto-Bliesner, B., and Aerts, J. C. J. H.: Agreement between reconstructed and modeled boreal precipita-

tion of the Last Interglacial, Science Advances, 5, https://doi.org/10.1126/sciadv.aax7047, https://advances.sciencemag.org/content/5/11/eaax7047, 2019.

The HadGEM2 Development Team, Martin, G. M., Bellouin, N., Collins, W. J., Culverwell, I. D., Halloran, P. R., Hardiman, S. C., Hinton,
555   T. J., Jones, C. D., McDonald, R. E., McLaren, A. J., O'Connor, F. M., Roberts, M. J., Rodriguez, J. M., Woodward, S., Best, M. J.,
Brooks, M. E., Brown, A. R., Butchart, N., Dearden, C., Derbyshire, S. H., Dharssi, I., Doutriaux-Boucher, M., Edwards, J. M., Falloon,
P. D., Gedney, N., Gray, L. J., Hewitt, H. T., Hobson, M., Huddleston, M. R., Hughes, J., Ineson, S., Ingram, W. J., James, P. M., Johns,
T. C., Johnson, C. E., Jones, A., Jones, C. P., Joshi, M. M., Keen, A. B., Liddicoat, S., Lock, A. P., Maidens, A. V., Manners, J. C., Milton,
S. F., Rae, J. G. L., Ridley, J. K., Sellar, A., Senior, C. A., Totterdell, I. J., Verhoef, A., Vidale, P. L., and Wiltshire, A.: The HadGEM2
560   family of Met Office Unified Model climate configurations, Geoscientific Model Development, 4, 723–757, https://doi.org/10.5194/gmd-4-723-2011, https://www.geosci-model-dev.net/4/723/2011/, 2011.

Tzedakis, P. C., Drysdale, R. N., Margari, V., Skinner, L. C., Menviel, L., Rhodes, R. H., Taschetto, A. S., Hodell, D. A., Crowhurst, S. J.,
Hellstrom, J. C., Fallick, A. E., Grimalt, J. O., McManus, J. F., Martrat, B., Mokeddem, Z., Parrenin, F., Regattieri, E., Roe, K., and
Zanchetta, G.: Enhanced climate instability in the North Atlantic and southern Europe during the Last Interglacial, Nature Communica-
565   tions, 9, 4235, https://doi.org/10.1038/s41467-018-06683-3, 2018.

Valcke, S.: The OASIS3 coupler: a European climate modelling community software, Geoscientific Model Development, 6, 373–388,
https://doi.org/10.5194/gmd-6-373-2013, https://www.geosci-model-dev.net/6/373/2013/, 2013.

Wang, B., Kim, H.-J., Kikuchi, K., and Kitoh, A.: Diagnostic metrics for evaluation of annual and diurnal cycles, Climate Dynamics, 37,
941–955, https://doi.org/10.1007/s00382-010-0877-0, 2011.

570   Wang, Y.-P. and Leuning, R.: A two-leaf model for canopy conductance, photosynthesis and partitioning of available energy I:: Model
description and comparison with a multi-layered model, Agricultural and Forest Meteorology, 91, 89–111, https://doi.org/10.1016/S0168-1923(98)00061-6, http://www.sciencedirect.com/science/article/pii/S0168192398000616, 1998.

Wang, Y. P., Law, R. M., and Pak, B.: A global model of carbon, nitrogen and phosphorus cycles for the terrestrial biosphere, Biogeosciences,
7, 2261–2282, https://doi.org/10.5194/bg-7-2261-2010, https://www.biogeosciences.net/7/2261/2010/, 2010.

575   Yau, A. M., Bender, M. L., Robinson, A., and Brook, E. J.: Reconstructing the last interglacial at Summit, Greenland: Insights from GISP2,
Proceedings of the National Academy of Sciences, 113, 9710, https://doi.org/10.1073/pnas.1524766113, http://www.pnas.org/content/113/35/9710.abstract, 2016.

Ziehn, T., Chamberlain, M. A., Law, R. M., Lenton, A., Bodman, R. W., Dix, M., Stevens, L., Wang, Y.-P., and Srbinovsky, J.: The Australian
Earth System Model: ACCESS-ESM1.5, Journal of Southern Hemisphere Earth Systems Science, 70, 193–214, https://doi.org/10.1071/ES19035, 2020.
580
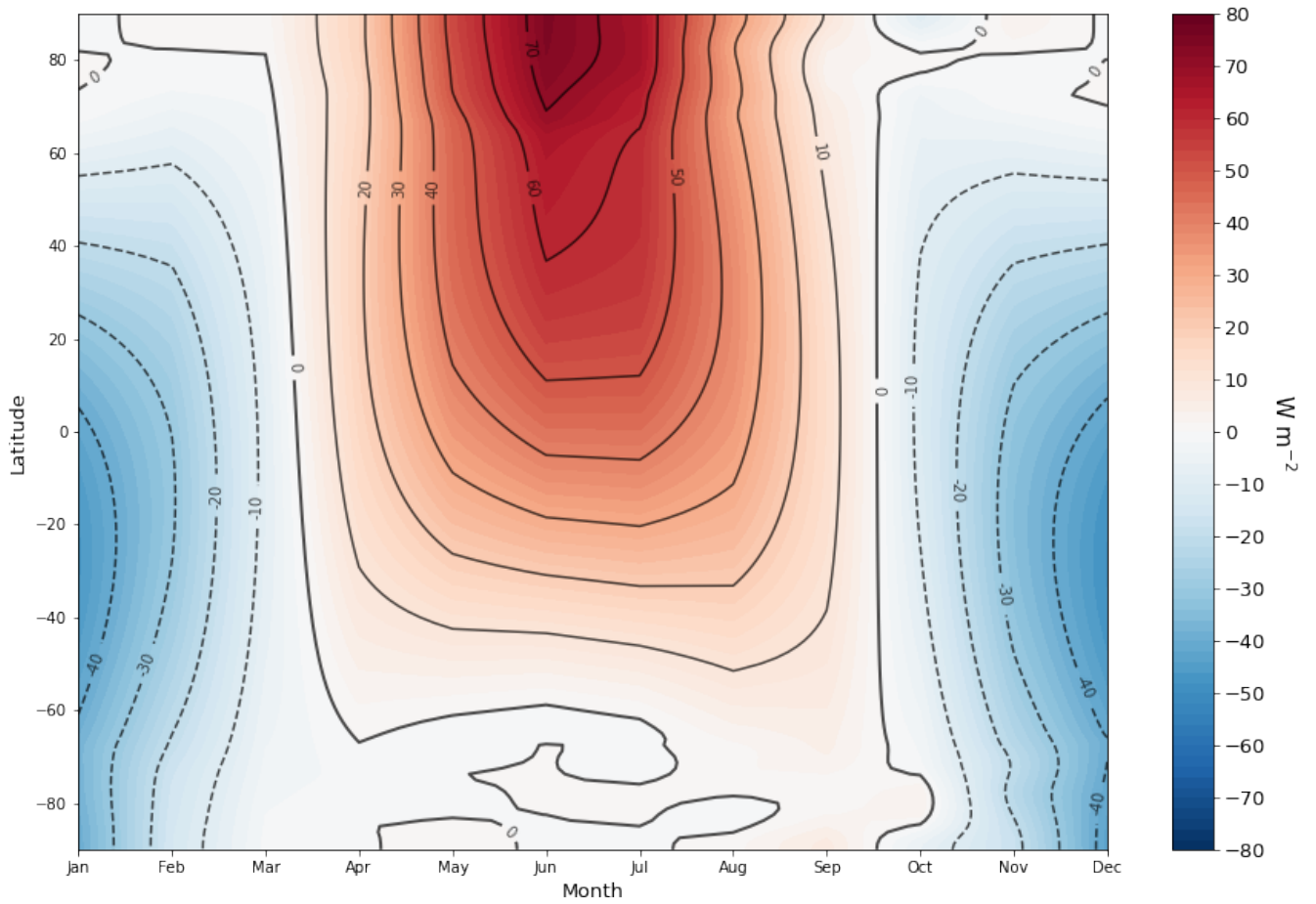
Figure 1. Monthly insolation anomalies at LIG compared to PI. The lengths of months are adjusted using a "fixed-angular" definition following Bartlein and Shafer (2019) (See section 2.2).
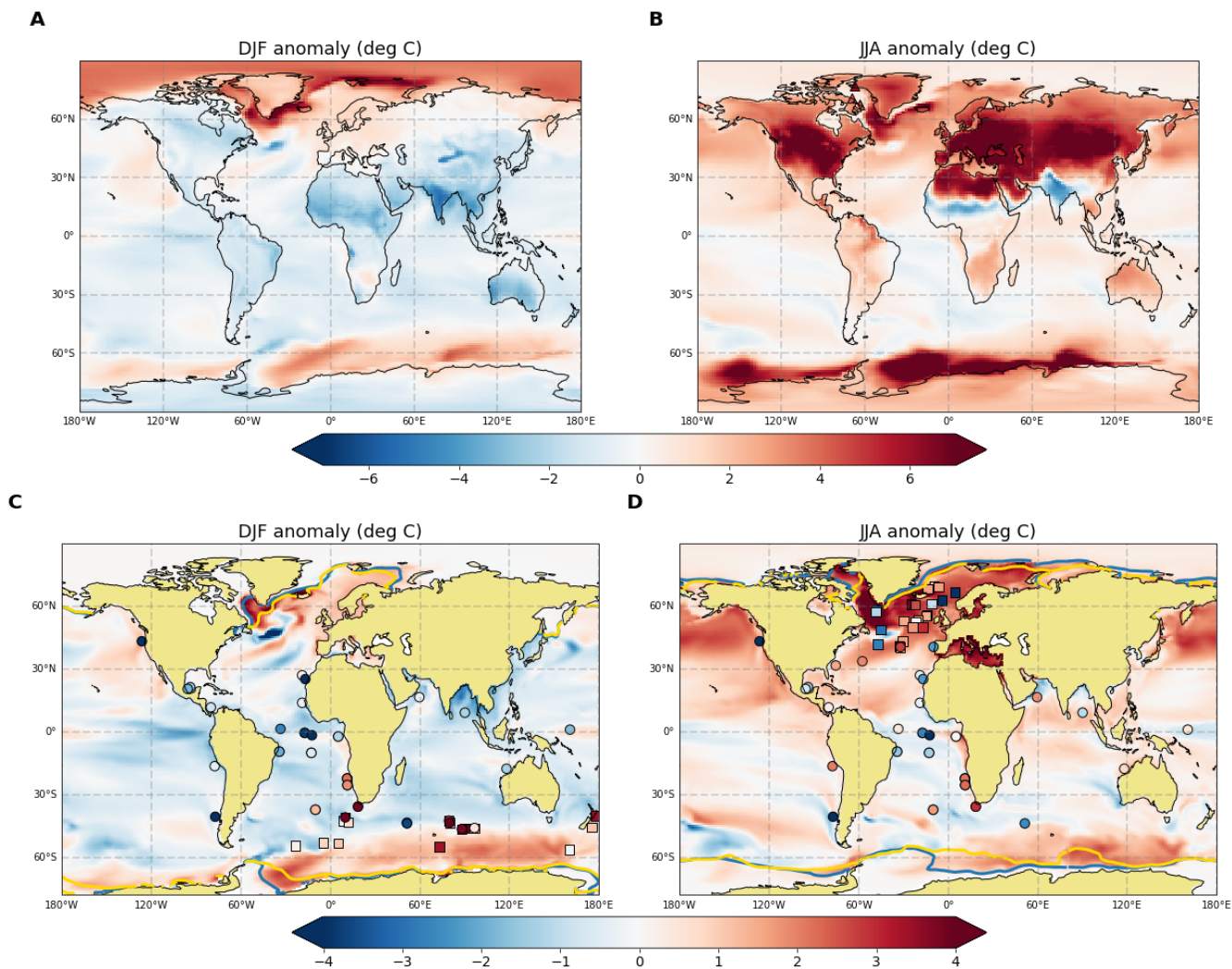
Figure 2. DJF and JJA surface temperature anomalies (LIG minus PI) with proxy data overlaid (filled markers: squares for the compilation by Capron et al. (2014, 2017); dots for the compilation by Hoffman et al. (2017); triangles for Arctic terrestrial proxies (Axford et al., 2011; Francis et al., 2006; Fréchette et al., 2006; McFarlin et al., 2018; Melles et al., 2012; Plikk et al., 2019; Salonen et al., 2018)). The preindustrial reference is 1850 CE for model anomalies, 1870–1899 for Capron et al. (2014, 2017) and 1870–1889 for Hoffman et al. (2017). (a)–(b): Surface air temperatures. (c)–(d): Sea surface temperatures, with contours of sea-ice concentration at 15 % overlaid in February for DJF and August for JJA (blue: LIG; yellow: PI).
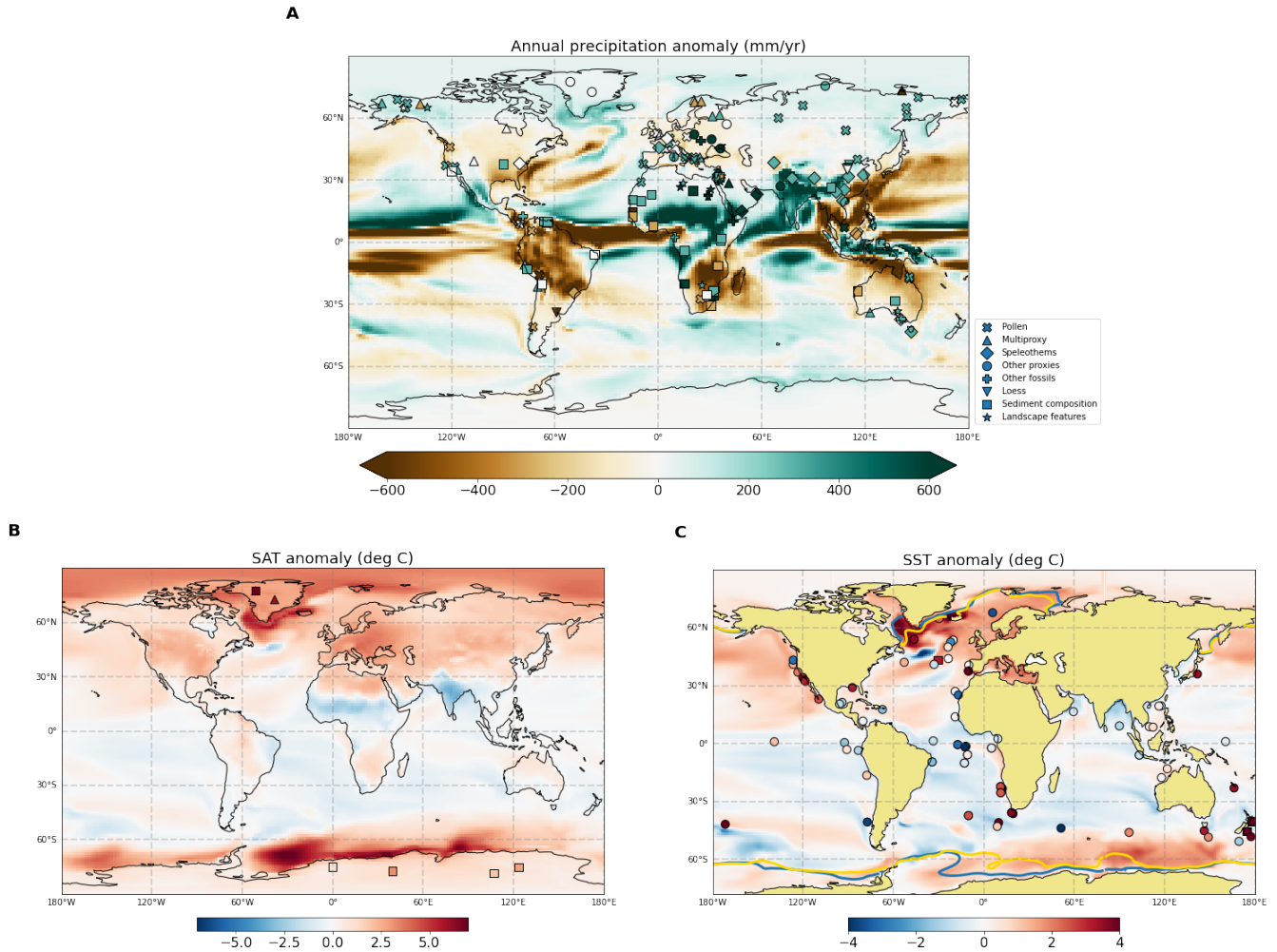
Figure 3. (a): Simulated annual mean precipitation anomaly (mm yr^{-1}) with proxy reconstructions from Scussolini et al. (2019) overlaid. Proxy reconstructions are semi-quantitative with much drier conditions shown in brown, drier in light brown, and the reverse for green. (b): Annual mean surface air temperature anomalies (°C) with proxy data (filled markers: squares for the compilation by Capron et al. (2014, 2017); triangles for Arctic terrestrial proxies (Landais et al., 2016; NEEM community members et al., 2013; Yau et al., 2016)). (c): Annual mean sea surface temperature anomalies with proxy data (filled markers: squares for the compilation by Capron et al. (2014, 2017); dots for the compilation by Hoffman et al. (2017)), and contours of annual sea-ice concentration at 15 % overlaid (blue: LIG; yellow: PI).
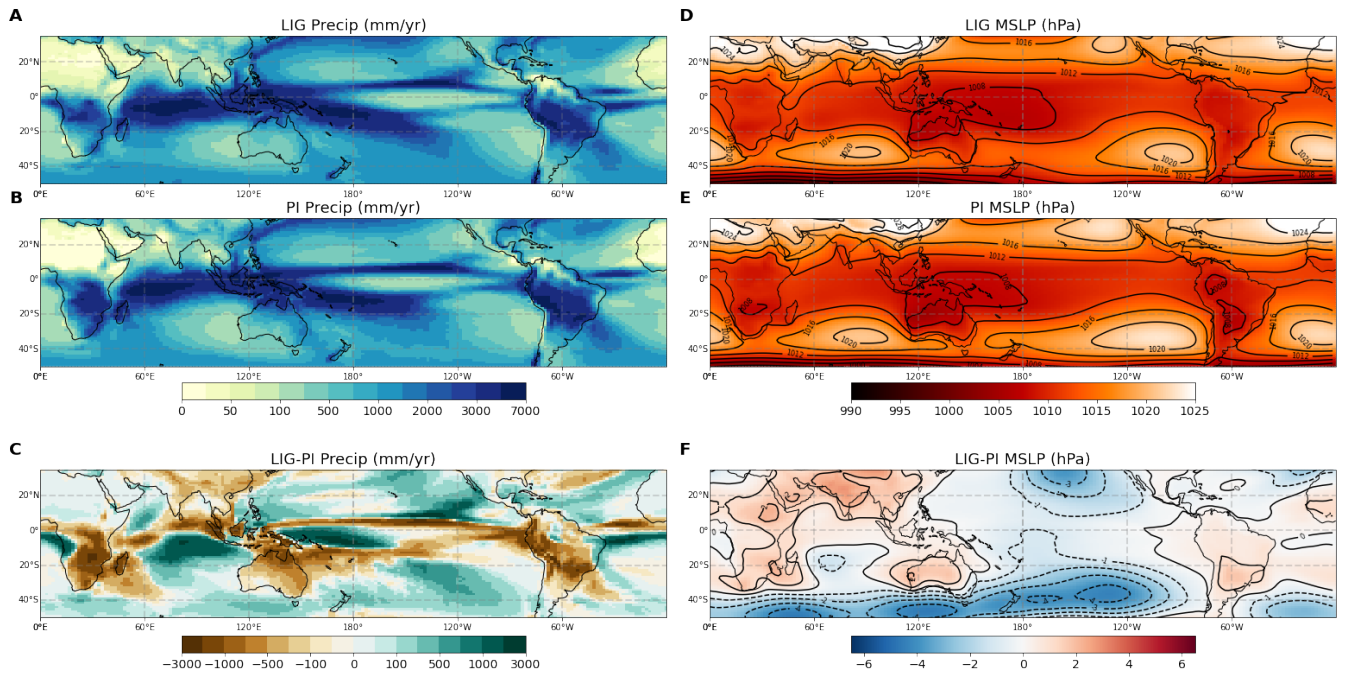
Figure 4. Left panels: Simulated DJF precipitation for (a) LIG, (b) PI and (c) LIG minus PI. Right panels: Simulated DJF mean sea level pressure (MSLP) for (d) LIG, (e) PI and (f) LIG minus PI.
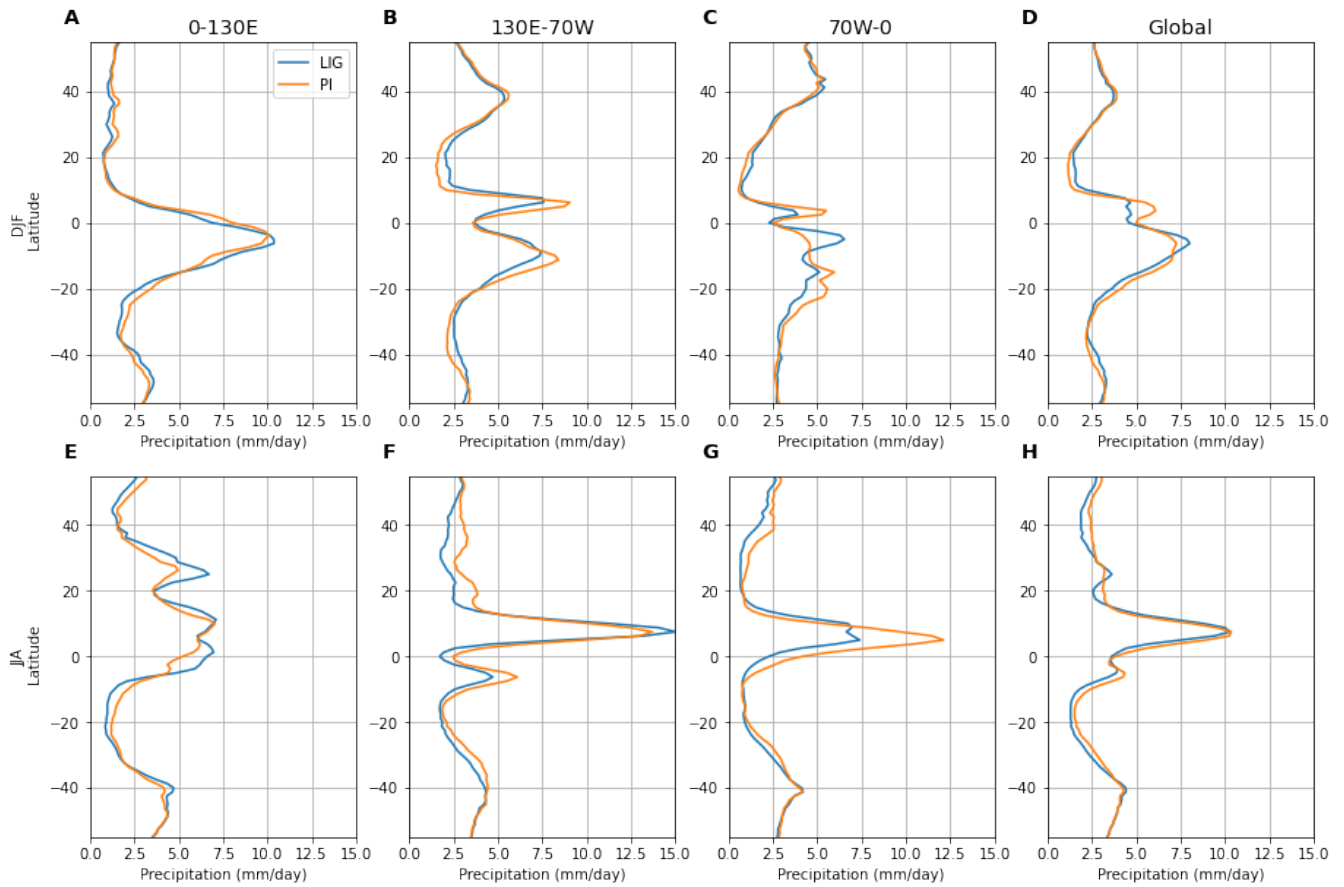
Figure 5. Zonally averaged precipitation (mm day^{-1}). 0°–130° E covers most of Africa, Indian Ocean, and up to Western Australia; 130° E–70° W covers the Pacific Ocean; and 70° W–0° covers the central part of Atlantic Ocean. (a)–(d): DJF; (e)–(h): JJA.
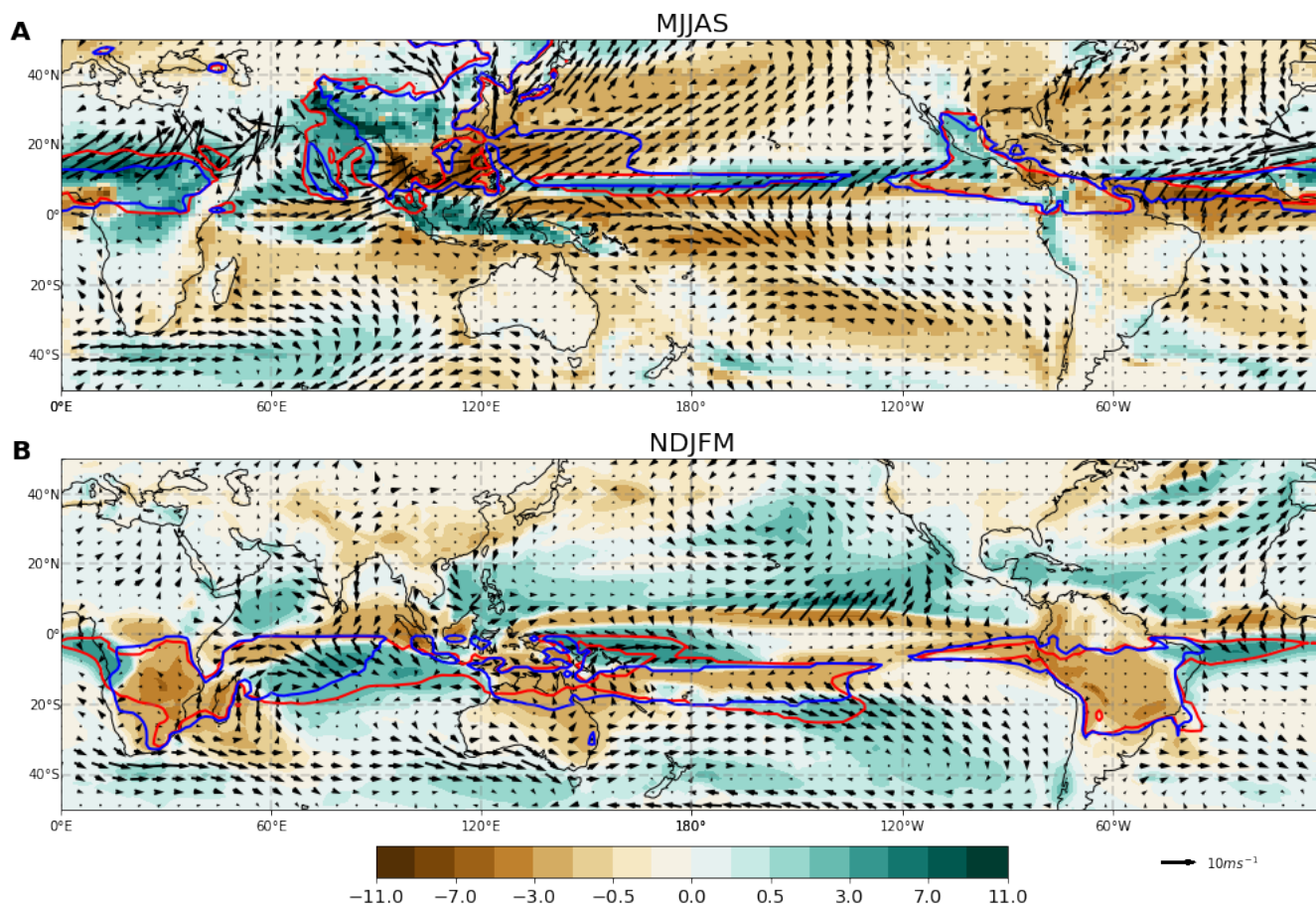
Figure 6. Precipitation anomaly (mm day^{-1}) with surface wind anomaly overlaid. (a): MJJAS; (b): NDJFM. Monsoon domains, defined as regions in which the precipitation during the monsoon season (NH: MJJAS; SH: NDJFM) is greater than the dry season (NH: NDJFM; SH: MJJAS) by at least 2.5 mm day^{-1} and responsible for at least 55% of the annual precipitation, are shown for the LIG (red contours) and for PI (blue contours).
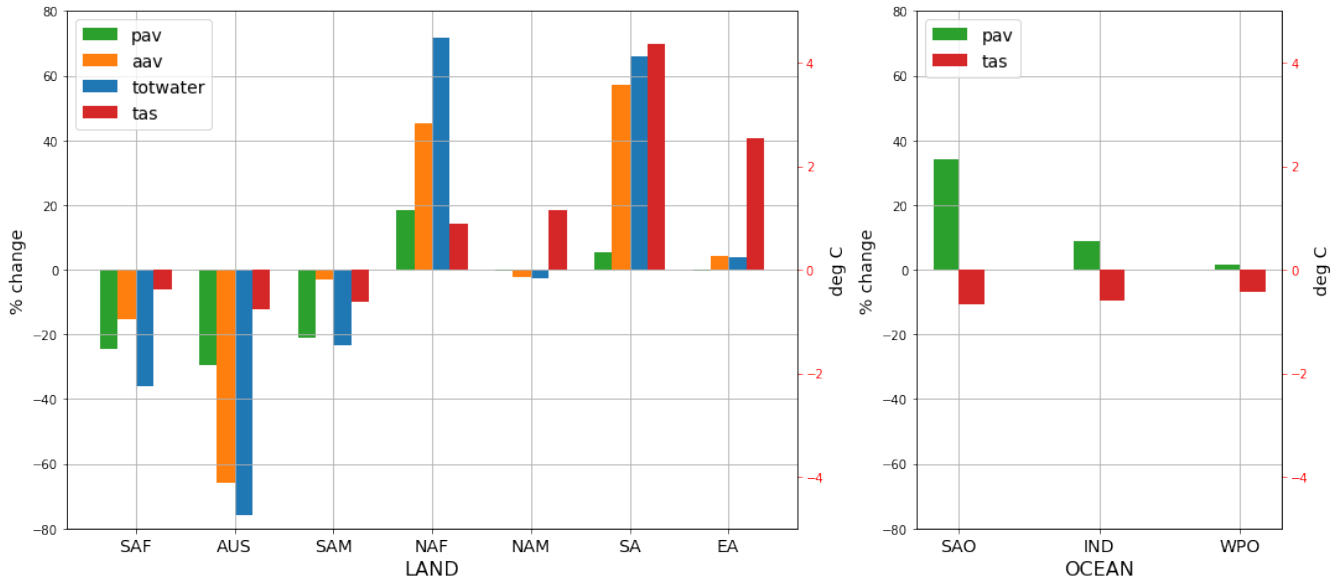
Figure 7. Changes in monsoon season (NH: MJJAS, SH: NDJFM) precipitation averaged within (left) terrestrial monsoon domains shown in Fig. 6 and (right) over SH ocean regions. Areas in which individual monsoon and ocean regions are bounded are defined in Table S1. Pav: Percentage change in area-averaged precipitation rate during monsoon season. Aav: Percentage change in areal extent of regional monsoon domain. Totwater: Percentage change in total precipitated water during monsoon season (mean precipitation rate over monsoon domain multiplied by areal extent). TAS: air surface temperature (in °C). Key: SAF = South African monsoon; AUS = Australian monsoon; SAM = South American monsoon; NAF: North African monsoon; NAM = North American monsoon; SA = South Asian monsoon; EA = East Asian monsoon; SAO = South Atlantic Ocean; IND = Southern Indian Ocean; WPO = Western to Central Equatorial Pacific Ocean.
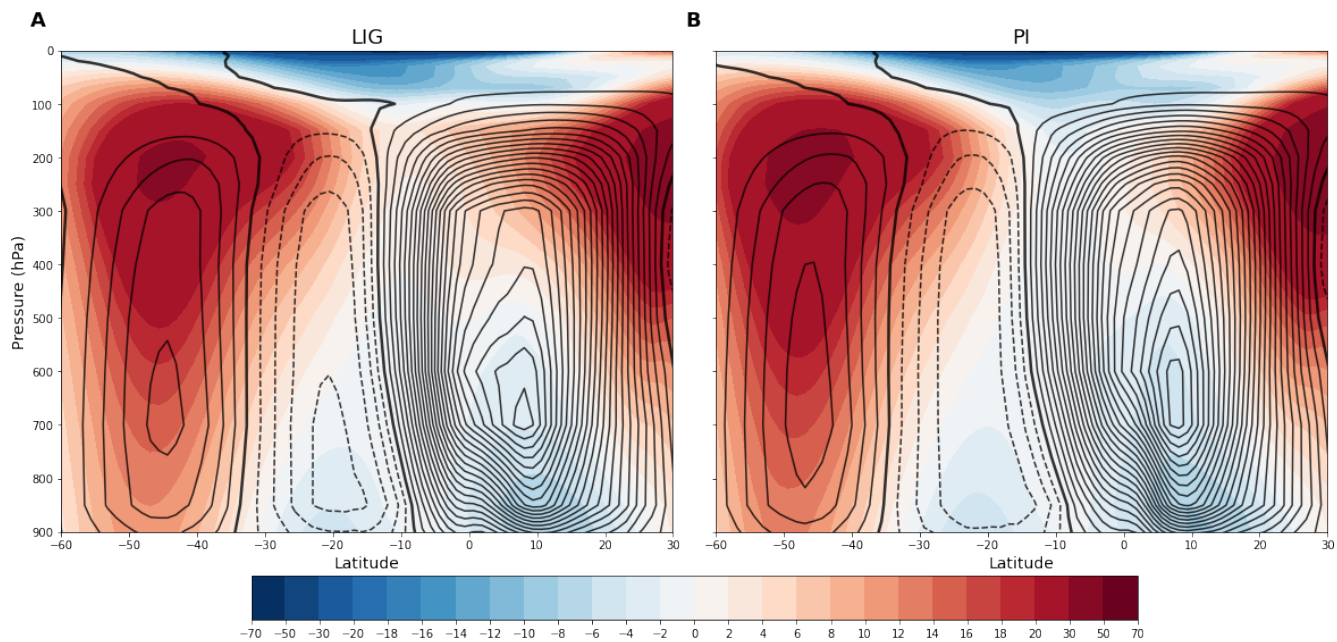
Figure 8. Atmospheric mass stream function in DJF, represented by solid (positive) and dashed (negative) contour lines, is contoured every 20 Sv, with the bold lines being the zero contours. Zonal mean zonal winds (m s^{-1}) are represented by colour shading. (a) LIG. (b) PI. Note the shading interval is not linear.

Table 1. Forcings and boundary conditions of the piControl and lig127k experiments.

	piControl (1850 CE)	lig127k (127 ka)
Orbital parameters		
Eccentricity	0.016764	0.039378
Obliquity (degrees)	23.459	24.040
Perihelion - 180	100.33	275.41
Vernal equinox	Fixed to noon on 21 March	Fixed to noon on 21 March
Greenhouse gases		
Carbon dioxide (ppm)	284.3	275
Methane (ppb)	808.2	685
Nitrous oxide (ppb)	273.0	255
Other GHGs	CMIP DECK piControl	0
Solar constant	TSI: 1365.65 W m^{-2} *	
Paleogeography	Modern	
Ice sheets	Modern	
Vegetation	CMIP DECK piControl	
Aerosols: dust, volcanic, etc.	CMIP DECK piControl	

*While the solar constant in the protocol for CMIP DECK piControl is 1360.747 W m^{-2}, both the piControl and lig127k experiments were integrated with 1365.65 W m^{-2} according to CMIP5-PMIP3 guidelines. This allows comparison between our piControl and our lig127k experiment.

Table 2. Model components of the ACCESS-ESM1.5.

Model component	Name	Resolution
Atmosphere	UM7.3	1.875° x 1.25°, with 38 vertical levels, extending to 40 km.
Land surface	CABLE2.4	Same horizontal resolution as atmosphere. Each grid cell comprises of 13 plant functional types (PFT). No dynamic vegetation, but interactive LAI. Biogeochemistry implemented by CASA-CNP module.
Coupler	OASIS-MCT	
Ocean	MOM5	Nominally 1° in horizontal, with latitudinal refinements around the Equator (0.33° between 10° S and 10° N) and the Southern Ocean (ranging from 0.25° at 78° S to 1° at 30° S). 50 vertical levels with a nominal 10 m thickness in the upper ocean.
Marine carbon cycle	WOMBAT	Same as MOM5
Sea ice	CICE4.1	Same as MOM5